



**HAL**  
open science

## Modelling precipitation hardening in an A356+0.5 wt%Cu cast aluminum alloy

Vladimir A. Esin, Anass Assadiki, Vladimir Esin, Rémi Martinez, Warren Poole, Georges Cailletaud

► **To cite this version:**

Vladimir A. Esin, Anass Assadiki, Vladimir Esin, Rémi Martinez, Warren Poole, et al.. Modelling precipitation hardening in an A356+0.5 wt%Cu cast aluminum alloy. *Materials Science and Engineering: A*, 2021, 819, pp.141450. 10.1016/j.msea.2021.141450 . hal-03476740

**HAL Id: hal-03476740**

**<https://hal.science/hal-03476740>**

Submitted on 13 Jun 2023

**HAL** is a multi-disciplinary open access archive for the deposit and dissemination of scientific research documents, whether they are published or not. The documents may come from teaching and research institutions in France or abroad, or from public or private research centers.

L'archive ouverte pluridisciplinaire **HAL**, est destinée au dépôt et à la diffusion de documents scientifiques de niveau recherche, publiés ou non, émanant des établissements d'enseignement et de recherche français ou étrangers, des laboratoires publics ou privés.



Distributed under a Creative Commons Attribution - NonCommercial 4.0 International License

# Modelling precipitation hardening in an A356+0.5wt.%Cu cast aluminum alloy

Anass Assadiki<sup>1</sup>, Vladimir A. Esin\*<sup>1</sup>, Rémi Martinez<sup>2</sup>, Warren J. Poole<sup>3</sup>,  
and Georges Cailletaud<sup>1</sup>

<sup>1</sup>MINES ParisTech, PSL University, Centre des Matériaux (CNRS UMR  
7633), Évry, France

<sup>2</sup>Linamar Corporation, Guelph, Canada

<sup>3</sup>The University of British Columbia, Vancouver, Canada

May 11, 2021

## Abstract

The behavior of a A356+0.5wt.%Cu alloy used to manufacture cylinder heads was studied. Samples were solutionized, quenched and aged at 200 °C for 0.1, 1, 10 and 100 hours. TEM characterization showed that for the short aging durations (up to 10 hours), the dominating hardening precipitates were  $\beta''$  rods, while for the long aging duration (100 hours), the dominance shifted to the Q-phase ( $Q'$ ,  $Q''$  precipitates). The length and diameter of the  $\beta''$  rods were measured to produce size distributions which were later used to calibrate and validate the precipitation model. The physics-based precipitation kinetics model relies on classical nucleation/growth/coarsening equations adapted for the precipitation of Mg-Si precipitates in the aluminum matrix. Indirect coupling to Thermo-Calc software was used in order to determine the essential thermodynamic variables such as the driving force for precipitation and the solubility product for the model. Recent developments regarding the correction of the growth rate equations and the curvature effect were used to take into account the elongated morphology of precipitates. A Kampmann-Wagner Numerical (KWN) based model was used to track the evolution of the size distributions during nucleation, growth and coarsening of the  $\beta$  precipitates. The yield strength of the alloy was modelled using the Pythagorean sum of the contributions of intrinsic strength, solid solution strengthening and precipitation hardening. Both models showed good accuracy when compared to experimental results.

**Keywords:** Cast aluminum alloy; precipitation hardening; Thermo-Calc; KWN; yield stress; multi-physics modelling

---

\*Corresponding author: V.A. Esin (vladimir.esin@mines-paristech.fr)

# 1 Introduction

Light weighting, in conjunction with smaller and more efficient internal combustion engines, has resulted in drastic reduction of emissions by automobiles. These developments have pushed the substitution of steel and cast iron with lighter metals such as aluminum and magnesium alloys [1].

The topic of small, light and economical engines has been the main driving force in the use of cast aluminum alloys in the automotive industry. Since the end of the 90's, large, heavy and complex parts such as engine blocks and cylinder heads have been made using cast aluminum alloys. Casting such parts has led to the development of innovative casting process such as the tilted or the rotary gravity semi-permanent processes. Meanwhile, more conventional processes such as static gravity, low pressure and high pressure die casting have been optimized. Cast aluminum alloys draw their mechanical properties from precipitation hardening which is a diffusion controlled process. Understanding the interaction of heat treatment cycles with aging of the microstructure and the subsequent evolution of the mechanical properties helps design high-performance and safe parts with the use of advanced processes.

In order to achieve these goals, two types of modeling approaches have been developed since the early 2000's:

- The phenomenological approach. It is a single-scale model consisting in the introduction of several internal variables into the constitutive equations of a finite element model [2, 3]. It is an empirical, and therefore without a physics basis, but easy to implement which offers the advantage of low calculation costs but requires extensive testing in order to validate.
- The multiscale microstructure-informed approach which belongs to the field of Integrated Computational Materials Engineering (ICME) [4]. This approach is based on the equations of physics and aims to bridge the gap between microstructural changes and evolution of mechanical properties. Therefore, it allows the simulation of more complex thermal histories [5–9]. We can mention here as well the works which used phase field method [10, 11] as those based on first principles and Monte-Carlo simulations [12, 13]. This type of model presents the advantage of being more versatile and predictive but comes at a higher calculation costs.

The aim of this work is to improve an existing multiscale microstructure-informed approach in order to refine the prediction of the mechanical properties of a A356+0.5wt.%Cu aluminum alloy used to manufacture cylinder heads. The modelling effort starts at the nanoscale, with a precipitation model of non-spherical particles into the aluminum matrix following on work done by Martinez et al. for A319 type alloys [14]. A coupling of the precipitation model with an *areal-glide* dislocation model is then made at a microscale in order to determine the yield strength of the alloy. The outputs of both models are compared to transmission electron microscopy and tensile tests results.

## 2 Studied A356+0.5wt.%Cu alloy

The alloy investigated in this study is a primary A356+0.5wt.%Cu. Its chemical composition is presented in Table 1. The actual composition was measured using spark ionization mass spectrometry and was averaged over multiple areas in a sample.

Table 1: Chemical composition (wt. %) of the studied A356+0.5wt.%Cu alloy: nominal and measured using spark ionization mass spectrometry.

	Si	Cu	Mg	Sr	Fe	Ti	Other
Nominal	7	0.5	0.3	0.01	< 0.15	< 0.15	< 0.1
Measured	6.63	0.52	0.36	0.0067	0.114	0.136	0.054

Figure 1 shows a plot of the volume fraction of the different phases as a function of temperature obtained using Thermo-Calc software and TCAL5 database. The solvus temperature of the  $\beta$ -Mg<sub>2</sub>Si is 446 °C, thus defining the solution heat treatment temperature window between 446 and 562 °C, *i.e.* the solidus temperature. Solvus temperatures of the phases as given by Thermo-Calc are compared to values from literature in Table 2. This is used to validate the representativeness of the TCAL5 database for the studied alloy. Figure 1 shows that up to temperatures of 407 °C, the Q-phase is the stable phase, which is in good agreement with the literature [3, 15–19]. It can also be observed that the  $\theta$ -Al<sub>2</sub>Cu phase can coexist with the Q-phase at low temperature (< 266 °C).

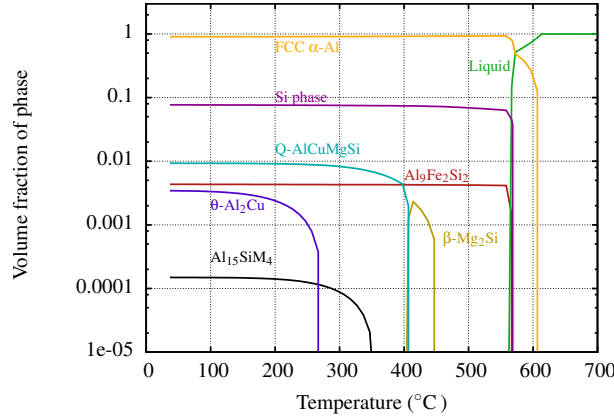


Figure 1: Volume fraction of phases as a function of temperature for an A356+0.5wt.%Cu alloy calculated with Thermo-Calc using the TCAL5 database.

Table 2: Comparison between calculated solvus temperatures of phases using the TCAL5 database and experimental values from literature.

Phases	Solvus temperature of phase (°C)		References
	TCAL5	Literature	
$\beta$ -Al <sub>9</sub> Fe <sub>2</sub> Si <sub>2</sub>	566	567.2	[3, 16]
Si	568	577.9	[17]
Q-phase	407	421.5	[18]
$\beta$ -Mg <sub>2</sub> Si	446	441.3	[19]

The samples were extracted from AFNOR<sup>1</sup> normalized cast aluminum alloy specimens. In this study the alloy was solutionized at around 500 °C, water quenched and then artificially aged at 200 °C for durations of 0.1, 1, 10 and 100 hours. The solutionizing heat treatments were conducted in a salt bath (60 % wt. KNO<sub>3</sub> + 40 % wt. NaNO<sub>2</sub>), while the artificial aging treatments were conducted in an oil bath. The use of baths for

<sup>1</sup>Association Française de NORmalisation (French Normalization Association)

the heat treatments allows a more efficient and homogeneous heat transfer ensuring a uniform temperature in the samples during cooling.

### 3 Precipitation characterization

After the heat treatment, the precipitates were characterized using transmission electron microscope (TEM) in order to investigate the precipitate structure and to produce size distributions which will be further used to validate the precipitation model.

For each of the studied aging conditions, first, small sections of material were cut from the bulk and were mechanically polished to a thickness of 80-100  $\mu\text{m}$ . Then, the samples were twin-jet polished using a 30% nitric acid + 70% methanol solution, at 15 V in a temperature range of -30 to -40  $^{\circ}\text{C}$ . The obtained thin foils were examined at the Canadian Centre for Electron Microscopy (CCEM) the McMaster University (Ontario, Canada) using a Philips CM-12 transmission electron microscope operated at 120 kV.

The  $\beta$  precipitates form along the  $\langle 001 \rangle$  directions of the FCC pro-eutectic  $\alpha$ -phase. Therefore, in order to observe them the aluminum matrix was oriented along the  $\langle 001 \rangle_{\alpha}$  zone axis.

#### 3.1 Nature and morphology

Figure 2 displays bright and dark field micrographs alongside with the corresponding selected area diffraction (SAD) patterns for samples aged at 200  $^{\circ}\text{C}$  with a  $\langle 001 \rangle_{\alpha}$  zone axis.

For 0.1 h of aging, a large number of very fine and homogeneously distributed precipitates is observed thanks to their roughly circular cross section (Figures 2a and e). The corresponding SAD pattern (Figure 2i) exhibits streaks of diffuse spots parallel to the  $\langle 100 \rangle_{\alpha}$  directions. The fine precipitates and the SAD pattern are in agreement with coherent rod-shaped short  $\beta''$  precipitates. Although the SAD pattern points to the presence of short and elongated precipitates, their edge section is not observable on the micrographs. It is worth noting that the chemical composition of the  $\beta''$  phase has an average atomic number close to aluminum and thus, chemical contrast is almost negligible. The edge section of the  $\beta''$  precipitates is visible thanks to the strain field around the precipitates which is due to the misfit between the precipitates and the aluminum matrix. Since the duration of the artificial aging applied to these samples was only 6 minutes, the precipitates are still in the early formation stage and their length is small. Therefore, the strain field induced in the matrix is weak which results in a low contrast and a more complicated observation. Moreover, the presence of Guinier-Preston zones cannot be excluded at this stage of aging.

For the samples aged for 1 h, a large number of fine and homogeneously distributed precipitates can be observed (Figures 2b and f). The corresponding SAD pattern (Figure 2j) exhibits streaks of sharp spots parallel to the  $\langle 100 \rangle_{\alpha}$  directions. The precipitates are rod-shaped  $\beta''$  precipitates oriented along  $\langle 100 \rangle_{\alpha}$  directions. In these images, precipitates are presented with a roughly circular cross section and an elongated edge section. The longer duration of the artificial aging in this condition allows further growth of the precipitates. Therefore, their length is large enough to create a strong strain field in the matrix, making their observation easier than the 0.1 h samples.

After 10 h at 200  $^{\circ}\text{C}$ , a large number of relatively coarser and homogeneously distributed rod-shaped  $\beta''$  precipitates can be observed (Figures 2c and g). Moreover, it is

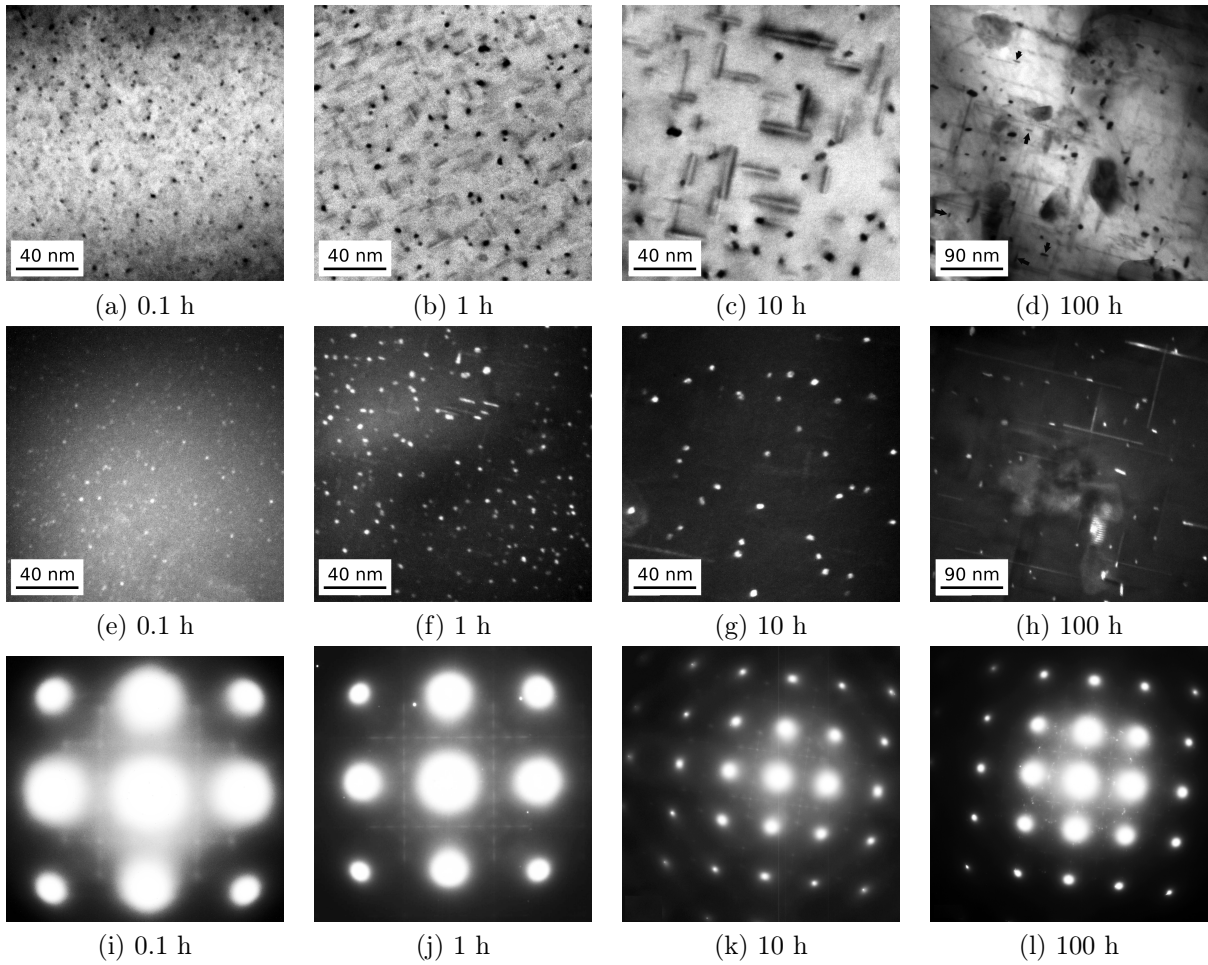


Figure 2: TEM observations along the  $\langle 001 \rangle_{\alpha}$  zone axis for samples of A356+0.5wt.%Cu alloy aged 0.1, 1, 10 and 100 h at 200 °C: (a) through (d) bright field images, (e) through (h) dark field images and (i) through (l) SAD patterns.

worth noting the coexistence of a different type of precipitates, present in a significantly smaller number. These lath-shaped precipitates display a rectangular cross section (BF images (Figure 2c) and have a longer length (DF images (Figure 2g)). This corresponds to the morphology of the Q'/Q'' phase [20, 21].

A more complex microstructure is observed after a 100 h aging period. Observations show a majority of fine lath-shaped precipitates with a roughly rectangular cross section (Figure 2d and h). Two families of precipitates can be observed: a majority of precipitates oriented at 10–12° from  $\langle 001 \rangle_\alpha$  directions, and a minority of other precipitates oriented along the  $\langle 001 \rangle_\alpha$  directions. The SAD pattern (Figure 2l) suggests that it is the Q' phase. Phases similar to the minority phase were observed in an AA6111 [22] and an Al-Si-Mg alloy with high Cu content [23] and were identified as Q'' and L respectively. Due to their small size, quantitative EDS measurements on these precipitates is not possible since some signal coming from the surrounding matrix is also detected. However, in comparison to the matrix it can be seen that these phases are rich in Al, Si, Mg and Cu. Thus, based on all these observations these lath precipitates are identified as majoritarily some Q' phase coexisting, in a smaller amount, with Q'' phase. Rod-shaped small precipitates are still observable but in a significantly lower number. Their low volume fraction is also reflected by their absence in the SAD pattern.

Table 3 presents a summary of the precipitates that were observed for each aging condition.

Table 3: Summary of the precipitates observed for each aging duration at 200 °C in the studied A356+0.5wt.%Cu alloy.

Duration (h)	$\beta''$	Q'/Q''
0.1	++++	absent
1	++++	absent
10	++++	+
100	+	++++

### 3.2 Distributions of size<sup>2</sup>

In addition to the identification of the nature of precipitates, quantitative measurements were performed in order to obtain the experimental distributions of size of the precipitates for each aging conditions. Length and diameter distributions of rod-shaped  $\beta''$  precipitates were created for samples aged at 200 °C during 0.1, 1 and 10 h.

It is important to note that it is not possible to measure the dimensions in more than one direction for the same precipitate due to their morphology and orientation. Thus, an average aspect ratio cannot be extracted. Instead, the mean aspect ratio is used in this study. The TEM images were imported into the commercial software ImageJ. After calibration, the precipitates were measured manually in order to characterize the size distributions. The latter are expressed as number fractions with respect to size bins of equal amplitude. For each distribution of size a total number, ranging from 285 to 520, of precipitates was measured. The experimental distribution of rod-shaped  $\beta''$  for each sample in terms of diameter and length is shown and discussed in Section 4.4 (Figure 8). As the duration of aging becomes longer, the growth process induces a size shift towards

<sup>2</sup>The distribution of size of the Q' phase (after 100 h of aging) is not investigated since this phase is disregarded in the study.

higher values. It is also noticeable that the distribution becomes wider and flatter due to aging. The average diameter evolves from 1 nm for an aging duration of 0.1 h to 2.8 nm for 10 h, and the average length evolves from 10.7 nm for an aging duration of 0.1 h to 20 nm for 10 h (Table 4). The aspect ratio of the 'average precipitate' shows a slight evolution from 6.3 to 7.1.

Table 4: Average length, diameter and aspect ratio of the  $\beta''$  precipitates obtained from TEM data after aging at 200 °C.

Duration (h)	Average length $\langle L \rangle$ (nm)	Average diameter $\langle D \rangle$ (nm)	Aspect ratio, $\lambda = \frac{\langle L \rangle}{\langle D \rangle}$
0.1	-	1.0±0.3	-
1	10.7±3.8	1.7±0.5	6.3
10	20.0±8.3	2.8±0.9	7.1

## 4 Precipitation kinetics model

Precipitation kinetics models usually focus on the description of three main processes: nucleation, growth and coarsening. Moreover, three different types of precipitation models can be found in literature: phase field, molecular dynamics and particle size distribution models. This study focuses on size distribution models, mostly for calculation efficiency.

The input variables to the precipitation kinetics model are the alloy composition, the thermal history and thermodynamic quantities such as the driving force for precipitation, equilibrium concentrations, etc. In the frame of this study, these variables were provided using an indirect coupling of the model with the Thermo-Calc software and the TCAL5 database. The model also uses a number of physical parameters such as the diffusivities of chemical elements. With the exception of the precipitate/matrix interfacial energy, the values of these parameters were provided by the literature. The value of the interfacial energy was used as a degree of freedom in order to obtain the best possible fit between the model and the measured distribution of sizes.

### 4.1 Nucleation

The approach used to model the nucleation of the precipitates is based on the classical nucleation theory. It starts with the expression of the variation of the Gibbs energy  $\Delta G$  resulting from the precipitation of a phase in a homogeneously supersaturated  $\alpha$  phase (aluminum based solid solution) (Eq. (1)):

$$\Delta G = \Delta g_v V + \gamma S. \quad (1)$$

The first half of the equation is volume related and consists in the volumetric chemical driving force for precipitation  $\Delta g_v$  and the volume  $V$  of the precipitating phase. The second half of the equation is surface related and depends on  $\gamma$ , the energy of matrix/precipitate interface, and the surface  $S$  of this interface. It is important to note that Eq. (1) can have a third term accounting for elastic strain energy. In this work this contribution is considered negligible and is therefore omitted.

The critical size of the nuclei  $R^*$ , *i.e.* the size at which a further growth will minimize the Gibbs energy, for a spherical shape of the precipitate is expressed by Eq. (2):

$$R^* = -\frac{2\gamma}{\Delta g_v}. \quad (2)$$

The energy barrier  $\Delta G^*$ , *i.e.* the free energy corresponding to a critical nucleus, can therefore be expressed using Eq. (3):

$$\Delta G^* = \frac{16\pi\gamma^3}{3\Delta g_v^2}. \quad (3)$$

The number of stable nuclei that are added to the system at any given time, in other words the nucleation rate  $J$ , is given by Eq. (4) [24, 25]:

$$J = Z\beta^*N \exp\left(-\frac{\Delta G^*}{k_B T}\right) \exp\left(-\frac{\tau}{t}\right) \quad (4)$$

with  $k_B$  being the Boltzmann constant and  $T$  the temperature. Generally, it is best viewed as the product of three factors. First, there is  $N \exp\left(-\frac{\Delta G^*}{k_B T}\right)$  which expresses the total number of nucleation sites which may lead to actual nucleation. On the one hand, it depends on the energy barrier which is temperature dependent. On the other hand,  $N$  represents the density of nucleation sites in the matrix. This study assumes a homogeneous nucleation, *i.e.* the absence of preferential nucleation sites within the matrix. Therefore,  $N$  can be expressed by Eq. (5) which considers that any atomic site in the crystal can be a potential nucleation site for the precipitating phase:

$$N = \frac{\mathcal{N}_A}{V^\alpha} \quad (5)$$

with  $\mathcal{N}_A$  being the Avogadro number and  $V^\alpha$  the molar volume of the matrix.

Second, the parameter  $Z\beta^*$  in Eq. (4) is known as the Zeldovitch factor. It is used to take into account the stochastic aspect of the nucleation process. Nuclei that are exactly at the energy barrier are unstable. They must either dissolve or grow. The expression of  $Z$  is given by Eq. (6):

$$Z = \frac{V^\alpha \Delta g_v^2}{8\pi(\gamma^3 k_B T)^{1/2}}. \quad (6)$$

The condensation rate  $\beta^*$  (Eq. (7)) expresses the rate at which “monomers” of the precipitating phase attached to the growing nuclei:

$$\beta^* = \frac{16\pi\gamma^2 D \bar{C}}{\Delta g_v^2 a^4} \quad (7)$$

with  $D$  being the solute diffusivity,  $\bar{C}$  the mean solute molar fraction in the matrix and  $a$  the lattice parameter of the matrix.

Third, the incubation of the nucleation process is expressed by  $\exp(-\tau/t)$ , where  $t$  is time. This term is used to simulate the thermal inertia of the nucleation process. The incubation period  $\tau$  expresses the time needed for the system to start the transformation. In reality, such a time is not a relevant for a constitutive equation.

A more rigorous approach would introduce a specific variable with its own evolution law that would be integrated as a function of the temperature history. In this work, back-to-back heat treat sequences of solutionizing, quenching and aging are simulated. The time dependency of incubation is therefore inconsistent with the above statement as phase

transformation may occur in different stages. In order to cover all possibilities, simulations were conducted with and without the incubation term and a negligible difference in the results. Therefore, it was decided not to use the incubation term in the final set of constitutive equations.

The evaluation of these equations requires the knowledge of the volumetric precipitation driving force  $\Delta g_v$  which depends on temperature and on the molar concentration of solute in the matrix. The molar concentration of solute in the matrix was obtained using Thermo-Calc and the TCAL5 database. It is worth noting that although the precipitates are identified as  $\beta''$ , the precipitation sequence is simplified to the equilibrium phase  $\beta$ -Mg<sub>2</sub>Si. Such an assumption finds its justification in the fact that in the TCAL5 database, thermodynamic data are more reliable when it comes to stable phases rather than metastable phases. It is assumed thus that the variation of  $\Delta g_v$  for  $\beta''$  has a similar temperature and composition dependence as  $\beta$ -Mg<sub>2</sub>Si. The input of these values from Thermo-Calc into the precipitation model is performed through an indirect coupling method. First, the values of the precipitation driving force of  $\beta$ -Mg<sub>2</sub>Si as a function of temperature and solute content in the matrix are tabulated. It was made sure that the ranges of temperature and composition encompass the ranges simulated in this study. Subsequently, all the results were mapped using a single Taylor function that was implemented into the model (Figure 3). The mathematical expression of the function is given by Eq. (8) where  $f$  is representing the driving force  $\Delta g_v$ ,  $x$  is representing the inverse of the temperature  $1/T(K)$ , and  $y$  is representing the logarithm of the molar fraction of Mg in the matrix  $\log(C_{Mg}^\alpha)$ .

$$\begin{cases} f(x, y) = ax^{-1} + by + cx^{-2} + dy^2 + eyx^{-1} + f \\ a = -3.65 \times 10^4 \text{ J m}^{-3} \text{ K}^{-1} \\ b = -1.03 \times 10^7 \text{ J m}^{-3} \\ c = -4.45 \times 10^2 \text{ J m}^{-3} \text{ K}^{-2} \\ d = -2.98 \times 10^4 \text{ J m}^{-3} \\ e = 4.46 \times 10^5 \text{ J m}^{-3} \text{ K}^{-1} \\ f = 2.04 \times 10^9 \text{ J m}^{-3} \end{cases} \quad (8)$$

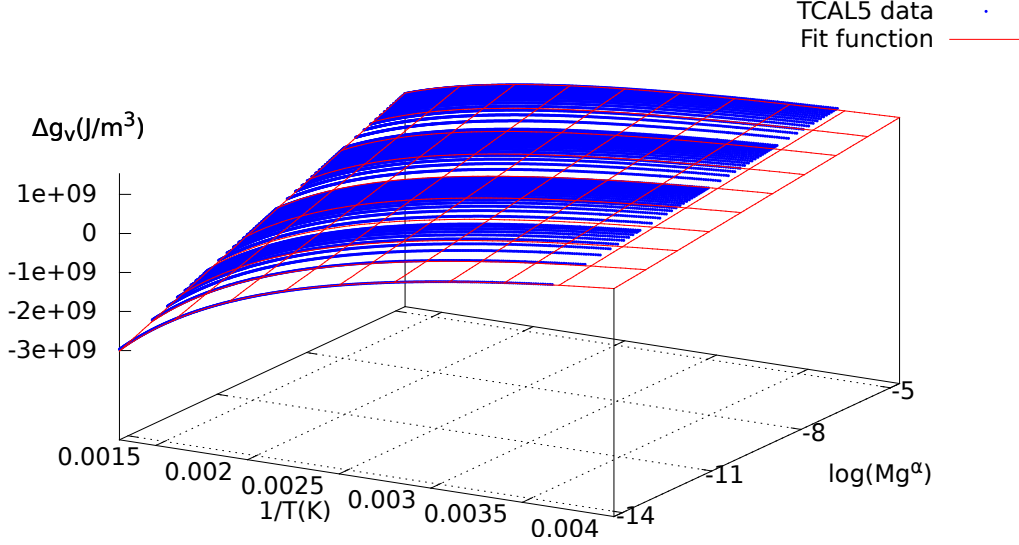


Figure 3: Fit function (Eq. (8)) of the precipitation driving force of  $\beta$ -Mg<sub>2</sub>Si in the aluminum matrix extracted from Thermo-Calc/TCAL5.

This indirect coupling method has the advantage of being efficient in terms of computation time when compared to a direct coupling to Thermo-Calc.

## 4.2 Growth

A stable supercritical nucleus ( $R > R^*$ ) is capable of growing into increasingly larger sizes. The growth rate of a stoichiometric  $\beta$ -Mg<sub>2</sub>Si precipitate (no diffusion within the precipitate) at a steady-state regime ( $\partial C_i / \partial t = 0$ ) is given by Eq. (9):

$$\frac{dR(t)}{dt} = f \frac{D_{Mg} (C_{Mg}^\infty - C_{Mg}^{\alpha/\beta})}{R(t) (C_{Mg}^\beta - C_{Mg}^{\alpha/\beta})} = f \frac{D_{Si} (C_{Si}^\infty - C_{Si}^{\alpha/\beta})}{R(t) (C_{Si}^\beta - C_{Si}^{\alpha/\beta})}, \quad (9)$$

where  $R$  represents the precipitate radius,  $D_i$  is the diffusion coefficient of element  $i$  in the matrix,  $C_i^\infty$  is concentration of element  $i$  in the matrix far from the interface,  $C_i^{\alpha/\beta}$  is concentration of element  $i$  in the matrix at the interface and  $C_i^\beta$  is the content of element  $i$  in the stoichiometric precipitate. The correction factor  $f$  takes into account the morphology of a non-spherical precipitate which is assumed to be approximated by a prolate spheroid (Figure 4) and can be obtained using the precipitate aspect ratio  $\lambda$  according to Holmedal *et al.* [26] (Eq. (10)):

$$f(\lambda) = \frac{2\sqrt{\lambda^2 - 1}}{\sqrt[3]{\lambda} \ln(2\lambda^2 + 2\lambda\sqrt{\lambda^2 - 1} - 1)}. \quad (10)$$

This factor degenerates to a value of 1 for spheres, *i.e.* when  $\lambda = 1$ .

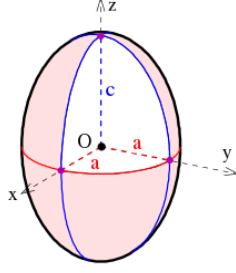


Figure 4: Prolate spheroid characterized by  $c > a$  approximating the rod shaped  $\beta''$  precipitates.

Eq. (9) implies that both Mg and Si diffusion fluxes in the aluminum matrix should give the same growth rate of  $\beta$  phase. This requires the addition of a thermodynamic and a kinetic constraints to fully define the growth rate.

The thermodynamic constraint consists of the tie-line equations in the Al-Si-Mg diagram expressing the equilibrium between  $\alpha$ -Al and  $\beta$  phase. Tie-lines are calculated using Thermo-Calc and TCAL5 database are shown in Figure 5a for temperatures ranging from 273.15 to 723.15 K. The solubility product  $K_s = (C_{Mg}^{\alpha,eq})^2 \cdot C_{Si}^{\alpha,eq}$  for the  $\beta$  phase is expressed as a function of the molar fractions of Mg and Si in the matrix at equilibrium,  $C_{Mg}^{\alpha,eq}$  and  $C_{Si}^{\alpha,eq}$  respectively. Therefore, plotting  $\log(K_s)$  against the inverse of the temperature bring these tie-lines into one straight line that can be fitted with a simple linear function (Figure 5b). The obtained fit equation expresses the thermodynamic constraint that the equilibrium concentrations must respect.

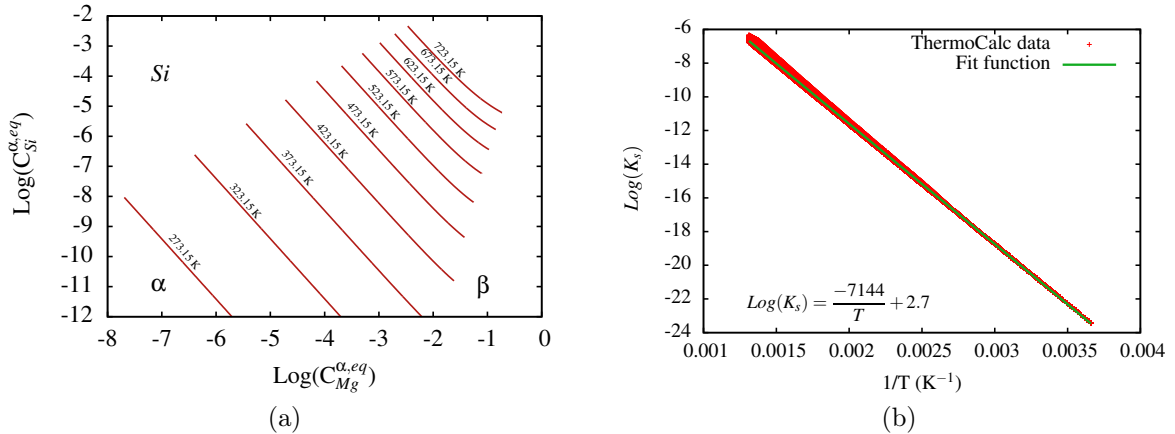


Figure 5: Determination of the solubility product for  $\beta$ - $\text{Mg}_2\text{Si}$  using Thermo-Calc software and TCAL5 database: (a) Mg and Si concentrations in the matrix for different temperatures representing the phase diagram tie-lines and (b) logarithm of the solubility product  $K_s$  as a function of the temperature inverse with the corresponding fit function implemented in the model.

The kinetic constraint comes by enforcing the fact that the flux of solute respects the difference in diffusivities between Mg and Si and of the stoichiometry of the precipitate. Therefore, the growth rate expressed by Eq. (9) must be the same whether it is calculated using the Mg or the Si supersaturation.

One of the simplifications used in this work is the collapse of the precipitation sequence into a single equivalent phase considered to be  $\beta$ - $\text{Mg}_2\text{Si}$ . The metastable precursors to

this phase are therefore not considered and all the aforementioned thermodynamic data are extracted from Thermo-Calc for the stable phase only. This simplification was used in the pioneering implementations of precipitation modelling by Myhr *et al.* [27, 28], Deschamps *et al.* [29] and Bréchet *et al.* [30]. Also, as mentioned previously, this phase is considered to be stoichiometric which is used to define the molar concentrations  $C_{Si}^\beta$  and  $C_{Mg}^\beta$  (0.334 and 0.666 respectively). The concentrations far from the interface  $C_{Mg}^\infty$  and  $C_{Si}^\infty$ , can be considered as the mean solute concentrations in the matrix at any given time step. Therefore, the remaining unknown parameters in order to evaluate the growth rate are the matrix interfacial concentrations  $C_{Si}^{\alpha/\beta}$  and  $C_{Mg}^{\alpha/\beta}$ .

In the case of a curved interface  $\alpha/\beta$ , the equilibrium between the two phases is modified due to capillarity effects. This is the Gibbs-Thomson effect. When assuming a local equilibrium modified by the Gibbs-Thomson effect, the interfacial compositions are the equilibrium compositions corrected for curvature. Indeed, the solute concentrations in the matrix near the  $\alpha/\beta$  interface and far from it are different. The classical expression that is used is given by Eq. (11):

$$C_{i,R}^{\alpha/\beta} = C_{i,R=\infty}^{\alpha/\beta} \exp\left(\frac{2\gamma V^\beta}{Rk_B T}\right), \quad (11)$$

with  $C_{i,R=\infty}^{\alpha/\beta}$  the concentration of solute  $i$  in the matrix for an infinite radius of curvature (planar interface),  $V^\beta$  the molar volume of the precipitating  $\beta$  phase and  $R$  the precipitate radius.

Although this expression is commonly used, it is worth noting that it is obtained by using an approximation that does not always apply to multi-component systems. Perez [31] showed that this solution of the Gibbs-Thomson equation is obtained under the assumption of a pure precipitating phase (*i.e.*  $C_i^\beta=1$ ).

By assuming a dilute solid solution approximation where  $C_{i,R}^{\alpha/\beta}$  and  $C_{i,R=\infty}^{\alpha/\beta}$  are small compared to 1, a modified Gibbs-Thomson equation can be determined (Eq. (12)) [26, 31]:

$$C_{i,R}^{\alpha/\beta} = C_{i,R=\infty}^{\alpha/\beta} \exp\left(\frac{2g\gamma V^\beta}{C_i^\beta Rk_B T}\right). \quad (12)$$

where  $g$  is the second correction factor used in order to take into account the non-spherical morphology of  $\beta$ -Mg<sub>2</sub>Si precipitates and which can be calculated using Eq. (13) [26]:

$$g(\lambda) = \frac{1}{2\lambda^{2/3}} \left(1 + \frac{\lambda^2}{\sqrt{\lambda^2 - 1}} \sin^{-1}\left(\frac{\sqrt{\lambda^2 - 1}}{\lambda}\right)\right), \quad (13)$$

Both  $f$  and  $g$  are correction factors which depend on the aspect ratio. A subsequent paper by Du *et al.* [32] used the correction factors to simulate an isothermal aging heat treatment on an Al-Mg-Si alloy. The authors performed three kinds of simulations: using the spherical assumption, using the correction factors along with a constant aspect ratio of 8 and using the correction factors along with a varying aspect ratio. The authors found that the introduction of the correction factors improved the agreement of the model with the TEM observations. The correction factors produce wider distributions when compared to the spherical approach. Varying aspect ratio produces a faster evolution of the mean radius in comparison to the constant aspect ratio case. This approach was reported to be working particularly well for long durations of aging.

Introducing both correction factors to the model results in a size-dependent competition between the acceleration of diffusion and the suppression of the supersaturation

allowed by the modified Gibbs-Thomson effect. In this work the aspect ratio was considered constant and equal to the average value obtained using the results of the TEM analysis ( $\lambda = 6.6$ ) as it was done in Refs. [6, 8].

Eq. (12) is used to take into account the Gibbs-Thomson effect as it is the most coherent with the shape of the modeled precipitates. As expected, setting  $C_i^\beta = 1$  in Eq. (12), makes Eq. (12) identical to Eq. (11).

It is worth noting that Du *et al.* [33] used a different approach to evaluate the effect of curvature on interfacial equilibrium concentrations. It consisted in constructing what the authors referred to as a ‘‘Gibbs-Thomson phase diagram’’ using Thermo-Calc. It is obtained by increasing the Gibbs free energy of the precipitating phase in the database by  $2\gamma\kappa V_m$ , with  $\kappa$  being the curvature and  $V_m$  the precipitate molar volume. The in-built energy minimization algorithm of Thermo-Calc then produces a new phase diagram taking into account the curvature. This calculation is then performed for the entire range of curvature values in order to produce the full curvature-dependent diagram. The model then uses a table look-up technique to navigate the diagram and access the required values.

Another approach was demonstrated in [34] where the authors numerically integrated the differential form of the curvature-modified equilibrium condition of a multi-component system. With knowledge of Gibbs energies of the matrix and the precipitating phase, they numerically integrated the tie-line equations with increments of curvature.

Finally, the solute concentrations in the matrix far from the interface,  $C_{Mg}^\infty$  and  $C_{Si}^\infty$ , are considered to be equal to the mean matrix concentrations. The initial mean composition of the matrix is considered to be the equilibrium composition at the solutionizing temperature. As the volume fraction of the precipitating phase increases, the mean composition is updated using the mass balance Eq. (14):

$$\bar{C}_i^\alpha = \frac{C_i^0 - f^\beta \cdot C_i^\beta}{1 - f^\beta}, \quad (14)$$

with  $\bar{C}_i^\alpha$  being the mean concentration in the matrix of solute  $i$ ,  $C_i^0$  its initial concentration,  $C_i^\beta$  its concentration in the precipitate and  $f^\beta$  the molar fraction of the  $\beta$  phase. Since Mg is only consumed to form  $\beta$ -Mg<sub>2</sub>Si precipitates (the formation of Q phase is neglected in this study) and since solutionizing temperatures are always higher than the solvus temperature,  $C_{Mg}^0$  is considered constant in the model and equal to the mean alloy content.

The same cannot be said about  $C_{Si}^0$  because Si contributes to the formation of both  $\beta$ -Mg<sub>2</sub>Si and the eutectic Si phase. This is shown in Figure 6 where the yellow dash dash dotted curve represents the equilibrium Si concentration in the matrix and the red curve the equilibrium molar fraction of the Si phase (eutectic Si), according to TCAL5 database. Below the  $\beta$ -Mg<sub>2</sub>Si solvus temperature, the amount of Si that is available to the formation of  $\beta$ -Mg<sub>2</sub>Si is not a constant and does not correspond to the mean Si content in the alloy, since Si required to form the eutectic phase has to be taken into account. Therefore,  $C_{Si}^0$  (blue short dashed curve in Figure 6) was obtained by eliminating the amount of Si that goes into the formation of the Si phase from the mean Si content in the alloy, and one can see that  $C_{Si}^0$  is temperature-dependent. It was fit and implemented in the model as such. The corresponding assumption is that as soon as Si phase is formed, the matrix is instantly depleted from Si.

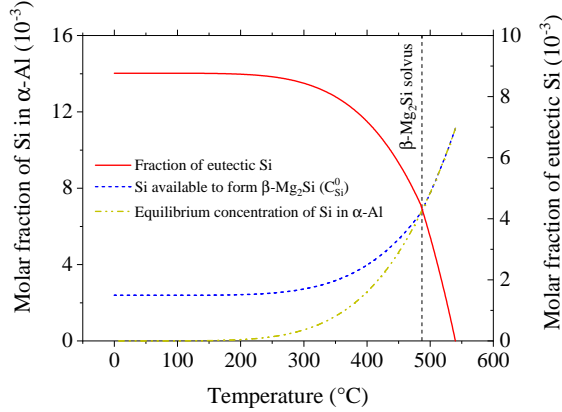


Figure 6: Concentration of Si available to form  $\beta$ -Mg<sub>2</sub>Si ( $C_{Si}^0$ ) (blue curve) with respect to temperature, obtained using the equilibrium concentration of Si in the aluminum matrix  $\alpha$  phase (yellow curve) and the molar fraction of the Si phase (eutectic Si) (red curve), calculated using Thermo-Calc software and TCAL5 database.

### 4.3 The KWN method

In order to track precipitation kinetics it is possible to solve the equation system outlined earlier for the mean radius (a single size class approach). This is less costly but requires defining an additional law when ripening takes over and the supersaturation is null. It can be achieved by using Lifshitz-Slyozov-Wagner (LSW) theory which specifies a critical radius between dissolving and growing particles. The model has to transition from one regime to the other based usually on arbitrary terms. Using a single size class approach also results in a loss of information regarding the shape of the size distribution and its width. This is especially of importance if this distribution to be used in a yield stress model. In such a model, it is desired to take into account the contribution of the entire distribution in impeding dislocation movement.

Another approach consists in uniformly discretizing the size space into a number of classes of size. This approach, referred to as the Kampmann-Wagner Numerical method (KWN) after [35], was successfully implemented in many studies [5, 6, 14, 27–29, 36]. The discretization of the continuous size distribution results in a number of size classes  $i$  of similar width  $\Delta R$  to which a number density  $\rho_i$  of particles of the same size  $R_i$  is associated. It is therefore possible to calculate the growth rate as expressed in Eq. (9) for each size class. The temporal evolution of the number density in any given size class therefore translates into a flux in the size space that must be defined. This constitutes one of the main advantages of the KWN method in tracking the evolution of size distributions of precipitates.

Another major advantage is its compatibility with nucleation theory. The size classes are filled using the particle flux described in the previous section. The model is therefore capable of handling the simultaneousness of the processes of nucleation and growth. It allows simulations of non-isothermal heat treatments where nucleation events can occur multiple times during the treatment. In addition to that, the transition to the ripening regime is done intrinsically. Even if the matrix supersaturation is close to 0, the Gibbs-Thomson effect still modifies the interfacial compositions in a size-dependent manner. Particles of small sizes dissolve and those with bigger sizes continue growing. It is also important to continuously evaluate the mean compositions as described earlier in order

to ensure mass conservation in the system.

Recall that central element of this model is the growth rate of the precipitating particles. In light of what was presented so far, the system of non linear equations consists of Eqs. (9) and (12) as well as the relation obtained for the solubility product  $K_s$  in Figure 5b. Solving this system for the growth rate relies on finding a set of equilibrium concentrations  $C_{Si}^{\alpha,eq}$  and  $C_{Mg}^{\alpha,eq}$  that satisfies the kinetic and thermodynamic constraints. This is achieved using a Newton-Raphson numerical resolution scheme.

Regarding the discretization of the size space, a minimum radius is introduced. Essentially, a particle for which the size is smaller than the lattice parameter is considered non-existent. The minimum radius is therefore set to 0.2 nm (*i.e.* a diameter of 0.4 nm, which is about one lattice parameter of aluminum at room temperature).

An adaptive time step management is also necessary in order to ensure that the solver respects a 1D Courant–Friedrichs–Lewy (CFL) type condition. This condition ensures that displacement in the size space, *i.e.* particles moving from one class to another, within the  $\Delta t$  timestep does not skip over classes. It is formulated according to Eq. (15):

$$\Delta t \leq \frac{\Delta R}{\dot{R}} \quad (15)$$

where  $\Delta R$  is the size space discretization step and  $\dot{R}$  the calculated growth rate.

Within the loop over the size classes, the maximum admissible value of the time step,  $\Delta t_{adm}$  is defined according to this condition. The timestep is therefore set with  $\Delta t = u\Delta t_{adm}$ ,  $u$  being a precision coefficient between 0 and 1. An upper limit,  $\Delta t_u$ , is systematically set to avoid large leaps in time when the condition allows it.

## 4.4 Simulation results

The parameters of the model and their values are compiled in Table 5. The diffusion coefficients for Mg and Si are assumed to be given by an Arrhenius law where  $Q_i$  is the activation energy and  $D_i^0$  its pre-exponential factor for the diffusion of element  $i$  in aluminum matrix. The interfacial energy  $\gamma$  is split into two values,  $\gamma^{nuc}$  applying for the nucleation theory equations and  $\gamma^{gro}$  applying for the Gibbs-Thomson effect. This was found to make the model more capable of handling the transition from nucleation/growth to coarsening.

There is a wide range of values in literature for the interfacial energies. In the publications where authors perform no comparison to experiments, this value is chosen arbitrarily within an acceptable range taking into account the nature of the phase and its coherence. In other publications where experiments are used as calibration, the values for the interfacial energy were chosen so as to give the best possible fit with experiments. In this work, the values for the interfacial energy were chosen in this manner. The simulated size distributions were compared to the experimental results.

Table 5: Summary of the precipitation model parameters for  $\beta$ -Mg<sub>2</sub>Si in aluminum matrix of A356+0.5wt.%Cu alloy and the values used in this work.

Model parameter	Symbol	Value	Unit	Source
$\alpha$ -Al lattice parameter	$a$	$4.05 \times 10^{-10}$	m	[37]
Molar volume of $\alpha$ -Al	$V_m^\alpha$	$1.02 \times 10^{-5}$	$\text{m}^3 \cdot \text{mol}^{-1}$	TCAL5 <sup>1</sup>
Molar volume of $\beta$ -Mg <sub>2</sub> Si	$V_m^\beta$	$1.29 \times 10^{-5}$	$\text{m}^3 \cdot \text{mol}^{-1}$	TCAL5 <sup>1</sup>
Activation energy for diffusion of Mg in $\alpha$ -Al	$Q_{Mg}$	120500	$\text{J} \cdot \text{mol}^{-1}$	[38]
Activation energy for diffusion of Si in $\alpha$ -Al	$Q_{Si}$	117600	$\text{J} \cdot \text{mol}^{-1}$	[38]
Pre-exponential factor of Mg diffusivity in $\alpha$ -Al	$D_{Mg}^0$	$1.49 \times 10^{-5}$	$\text{m}^2 \cdot \text{s}^{-1}$	[38]
Pre-exponential factor of Si diffusivity in $\alpha$ -Al	$D_{Si}^0$	$1.38 \times 10^{-5}$	$\text{m}^2 \cdot \text{s}^{-1}$	[38]
Molar fraction of Mg in $\beta$ -Mg <sub>2</sub> Si	$C_{Mg}^p$	0.666	-	Stoichiometry
Molar fraction of Si in $\beta$ -Mg <sub>2</sub> Si	$C_{Si}^p$	0.334	-	Stoichiometry
Interfacial energy for nucleation	$\gamma^{nuc}$	142	$\text{mJ} \cdot \text{m}^{-2}$	This work <sup>2</sup>
Interfacial energy for growth	$\gamma^{gro}$	54	$\text{mJ} \cdot \text{m}^{-2}$	This work <sup>2</sup>

<sup>1</sup>: averaged over temperatures between 20 and solutionizing temperature around 500 °C;

<sup>2</sup>: fit parameters.

To present the simulation results and compare them to the experiments, the model was given as input the same thermal history that was studied experimentally. It consists of quenching from a solutionizing temperature of around 500 °C down to room temperature with a cooling rate of 4.3 °C s<sup>-1</sup>, followed by a natural aging period and then heating to the aging temperature of 200 °C with a rate of 0.2 °C s<sup>-1</sup> and holding for 100 hours.

The response of the nucleation model is given in Figure 7a. The dotted lines refer to the end of quenching, the beginning of the heating ramp and the beginning of the aging heat treatment, respectively. It shows that the model predicts two nucleation peaks, the first one occurring during quenching and the second one in the middle of the heating ramp from room temperature to 200 °C. This explains the two-step observed in the total number density of precipitates, which is essentially the area under the nucleation peaks.

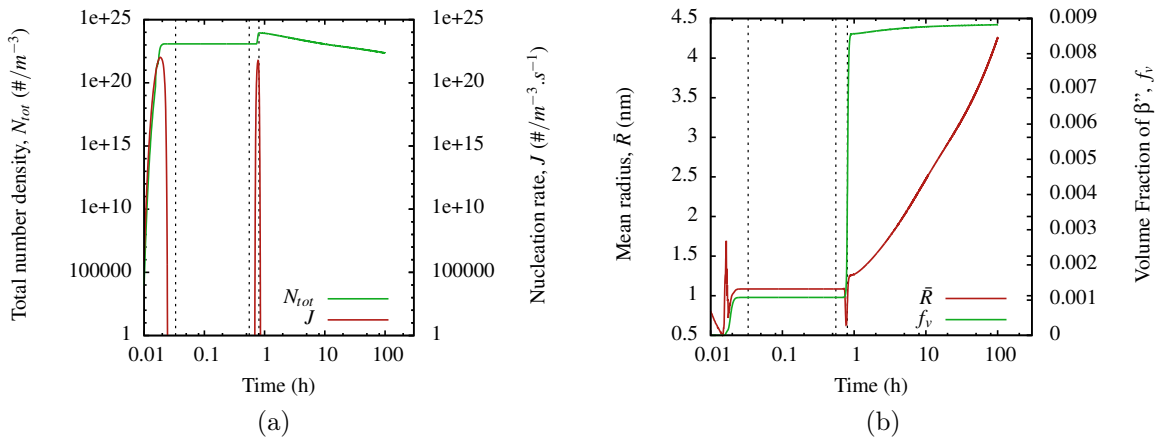


Figure 7: Simulated evolution of (a) the nucleation rate,  $J$ , and the total number density of precipitates,  $N_{tot}$  and (b) the mean radius,  $\bar{R}$ , and volume fraction,  $f_v$ , of the precipitating phase  $\beta''$ . The dotted lines refer to the end of quenching, the beginning of the heating ramp and the beginning of the aging heat treatment, respectively.

The effect of these two nucleation rate peaks can also be observed in Figure 7b. First, there is a two-step increase in the volume fraction which goes along with the evolution of

the total number density of precipitates. Then, the mean radius decreases twice as a result of the nucleation rate peaks. Indeed, with each nucleation rate peak, the system is flooded by a considerable number of precipitates of small size which explains the decrease observed for the main radius. According to Figure 7b, the volume fraction evolves following two steps. However, right after the second step, there seems to be an episode of pure growth without any nucleation events. Volume fraction later stabilises at a value close to 0.009 which is the equilibrium volume fraction of the  $\beta$ -Mg<sub>2</sub>Si phase predicted by Thermo-Calc at 200 °C (metastable calculation where the Q-phase is suppressed). This is in agreement with what was observed by Martinez *et al.* [14].

According to Figure 7a, it appears that coarsening starts to take place early in the aging heat treatment. Indeed the total number density of precipitates starts to decrease progressively as aging duration increases. There is however no clear distinction between the regimes of growth and coarsening. This can be explained by the fact that in the numerical conditions, equilibrium where the oversaturation is null and the volume fraction is constant is never reached.

As mentioned above, the interfacial energies were used as fitting parameters for the model. This fit was performed by qualitatively comparing the simulated and the experimental size distributions. The experimental size distributions were produced for the diameter and length of the rod shaped  $\beta''$  precipitates. It is worth noting that the diameter and length were not measured for the same particles (different TEM viewing directions). This means that what is referred to here as the average aspect ratio is the aspect ratio of the 'average particle' (*i.e.*  $\langle \lambda \rangle = \langle l \rangle / \langle D \rangle$ ).

In order to produce simulation variables comparable to the experiments, it is necessary to consider the volume of the rod shaped particle,  $V^{\text{rod}}$ , equal to the volume of a sphere of equivalent volume,  $V^{\text{SEV}}$  (Eq. (16)):

$$V^{\text{rod}} = V^{\text{SEV}}. \quad (16)$$

This leads to linking rod length  $l$  and diameter  $D$  to the radius of the sphere of equivalent volume  $R$  (*i.e.* the KWN radius) using Eqs. (17) and (18). A simulated length and diameter can therefore be obtained by using the value of the average aspect ratio given in the previous section ( $\lambda = 6.6$ ):

$$l = 2R \sqrt[3]{\frac{2}{3} \langle \lambda \rangle^2}, \quad (17)$$

$$D = 2R \sqrt[3]{\frac{2}{3 \langle \lambda \rangle}}. \quad (18)$$

The comparison between the experimental and simulated size distributions is given in Figure 8. Note that that size distribution of length for the 0.1 h aging duration was not determined experimentally. Overall, the model appears to be in agreement with the experiments. The early stages of aging (the 0.1 and 1 hour cases) are well represented. For the 10 h case, the model gives good agreement in terms of the mean radius and length. However, the model gives a narrower distribution of radius and length in comparison to the experiments. This may be the consequence of the assumption of a constant aspect ratio. Indeed, it was observed by Du *et al.* [32] that using a varying aspect ratio produced slightly wider size distributions.

In comparison with the results reported in the literature, to the best of our knowledge, the developed precipitation model is the first one which reliably describes the precipitation

kinetics in A356+0.5 wt. % cast alloy (a recent work by Chen et al. was devoted to Cu lean A356 alloy [8]). It successfully uses indirect coupling with Thermo-Calc to get the data on Si and Mg solubility, the driving force for  $\beta$ -Mg<sub>2</sub>Si precipitation, evolution of eutectic Si and molar volume for different phases. Actual precipitate morphology is described using the correction factors  $f$  and  $g$  calculated using aspect ratio  $\lambda$  which has not been done before for this type of alloys. The model can use any input thermal cycle to produce the size distribution of the precipitates.

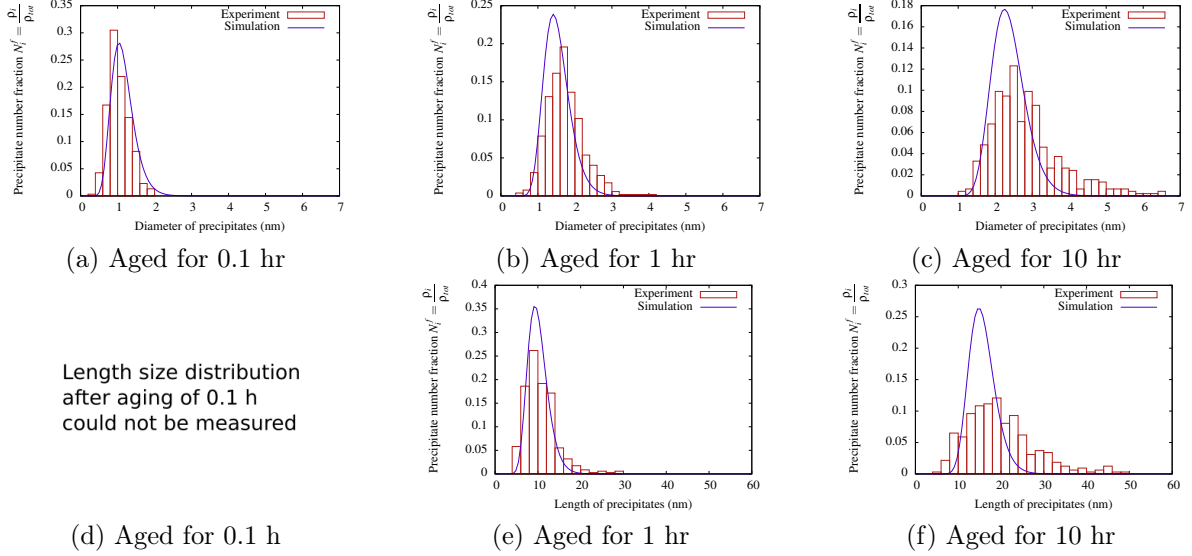


Figure 8: Comparison between the experimental and simulated size distributions of  $\beta''$  precipitates: (a), (b) and (c) diameter size distributions for aging durations of 0.1, 1 and 10 h respectively, (e) and (f) length size distributions for aging durations of 1 and 10 h at 200 °C, respectively.

## 5 Yield stress model

The precipitation model can be used to evaluate the yield stress of the studied A356+0.5wt.%Cu alloy, in principle, at any moment of any heat treatment using the micromechanical models available in the literature. A number of simplifications are however required to reduce complexity and calculation cost.

The yield stress of a representative volume element of the aluminum based solid solution ( $\alpha$  phase) is considered as the macroscopic yield stress of the alloy. This means that the effect of the eutectic constituent is not explicitly taken into account. There are multiple strengthening effects that contribute to the yield stress of the FCC matrix. The contribution of dislocation hardening is neglected since the alloy is cast and heat treated without any applied plastic deformation. The Peierls-Nabarro stress and the Hall-Petch effect are merged into a constant value  $\sigma_0$  which are chosen equal to 20 MPa. The contributions that are taken into account by the model are i) precipitation hardening and ii) solid solution strengthening. The superimposition of these contributions is done according to a simple additive rule given by Eq. (19) [39]:

$$\tau^q = \tau_1^q + \tau_2^q. \quad (19)$$

In this equation two contributions,  $\tau_1$  and  $\tau_2$  are summed according to a Pythagorean

law of exponent  $q$ . De Vaucorbeil *et al.* [39] used a dislocation line tension model to simulate the critical resolved shear stress (CRSS) obtained when combining two distributions of obstacles of different strength. It can be shown that when combining obstacle distributions of similar strength an exponent value of 2 should be used, and as the strength differential increases the exponent decreases to a value of 1.

Applying this to the hardening contributions that are taken into account in this work, the addition law for yield stress is thus written according to Eq. (20):

$$\sigma_y = \sigma_0 + \left( \sum_i \sigma_{i,ss}^2 \right)^{1/2} + (\sigma_{sh}^2 + \sigma_{by}^2)^{1/2}, \quad (20)$$

where  $\sigma_y$  is the yield stress,  $\sigma_{i,ss}$  is the individual solid solution strengthening contribution of element  $i$ ,  $\sigma_{sh}$  and  $\sigma_{by}$  are the contributions of shearable and bypassed precipitates respectively. The solid solution strengthening contributions of different elements are added with an exponent of 2 as they are considered similar. However, the overall addition rule uses an exponent of 1 as the difference between precipitation hardening, intrinsic strength and solid solution strengthening is significant.

The individual contribution of solid solution strengthening is taken into account according to Leyson *et al.* [40] using Eq. (21):

$$\sigma_{i,ss} = M k_i \bar{C}_i^{2/3}, \quad (21)$$

where  $M$  is the scale transition factor and  $\bar{C}_i$  is the mean molar fraction of element  $i$  in the matrix. Note that the selected value for  $M$  will correspond to an uniform stress model in the aggregate, which is reasonable for aluminum alloys at low strain. The authors of Ref. [40] determined the values of the coefficients  $k_i$  using first principles and the discrete Fourier transform method. They reported values of 342, 137, and 348 MPa/at%<sup>2/3</sup> for Mg, Si and Cu, respectively.

The strengthening effect due to precipitates is calculated by assessing the contributions of the entire size distribution as proposed by Deschamps *et al.* [41]. Contrary to a mean radius approach, this approach is able to factor in the width of distributions as well as bimodal distributions. The necessary stress,  $\sigma_p$ , required for a dislocation to glide through a distribution of precipitates in its glide plane is given by Eq. (22):

$$\sigma_p = \frac{M \bar{F}^p}{b \bar{L}}, \quad (22)$$

where  $\bar{F}^p$  is the mean precipitate strength and  $\bar{L}$  the average spacing between precipitates in the dislocation glide plane and  $b$  the Burgers vector magnitude.

The mean precipitate strength for a discretized size distribution of  $n$  classes can be written according to Eq. (23):

$$\bar{F}^p = \frac{\sum_i^n \rho_i F_i^p}{\sum_i^n \rho_i} \quad (23)$$

where  $\rho_i$  is the number density of precipitates in the size class  $i$  of radius  $R_i$  and strength  $F_i^p$ . The average strength of shearable and non-shearable precipitates  $\bar{F}_{sh}$  and  $\bar{F}_{by}$  can be written according to Eqs. (24) and (25) respectively:

$$\bar{F}_{sh} = k\mu b \frac{\sum_{i < i_c} \rho_i R_i}{\sum_{i < i_c} \rho_i}, \quad (24)$$

$$\bar{F}_{by} = 2\beta\mu b^2 \quad (25)$$

where  $i_c$  is the size class corresponding to the critical radius for shearing,  $R_{crit}$ ,  $\mu$  being the shear modulus and  $\beta$  being a scaling factor between 0.2 and 0.5.

The average precipitate spacing in the glide plane  $\bar{L}$  is determined by considering a cell as shown in Figure 9a [6, 9]. In this figure, three precipitates belonging to each family of orientation (the three  $[100]_\alpha$  directions) are positioned such that the spacing between them in the dislocation glide plane  $(111)$  is  $\bar{L}$  (Figure 9b).

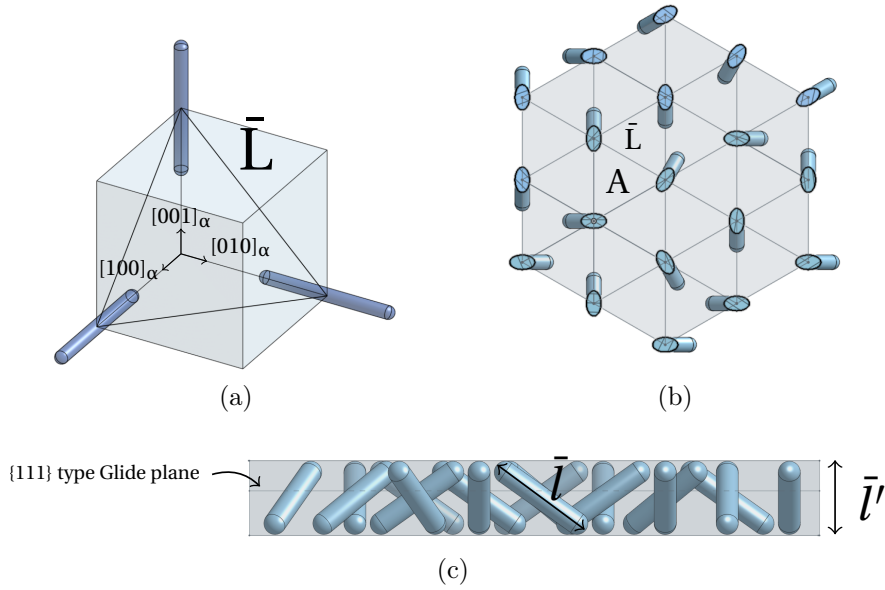


Figure 9: Schematic representation of the  $\beta''$  precipitates : (a) cell constituted of the three families of orientations, (b) a section view of a population of precipitates cut with the dislocation glide plane of  $\{111\}$  type and (c) side view of a population of precipitates of length  $\bar{l}$ .

One can obtain the expression of the average spacing (Eq. (26)):

$$\bar{L} = \sqrt{\frac{2}{\sqrt{3}\rho_A}}. \quad (26)$$

where  $\rho_A$  is the precipitate number density per unit area.

Figure 9c shows a population of precipitates of length  $\bar{l}$  with a total number density of  $\rho$  being intersected by the dislocation glide plane. The number density per unit area can therefore be written according to Eq. (27), where  $P$  is the probability of intersecting at any given height:

$$\rho = P\rho_A. \quad (27)$$

The probability  $P$  is simply  $1/\bar{l}'$ , where  $\bar{l}'$  is the height of the unit parallelepiped. This height is oriented along the [111] direction while  $\bar{l}$  is oriented along [100] direction. They are therefore linked according to Eq. (28):

$$\bar{l}' = \bar{l} \cos([111], [100]) = \frac{\bar{l}}{\sqrt{3}}. \quad (28)$$

Combining Eqs. (28) and (27) the number density per unit area can be expressed as follows:

$$\rho_A = \frac{\rho \bar{l}}{\sqrt{3}}. \quad (29)$$

Using  $\rho = \sum_i^n \rho_i$  and  $\bar{l} = \frac{\sum_i^n \rho_i l_i}{\sum_i^n \rho_i}$ , Eq. (26) writes :

$$\bar{L} = \sqrt{\frac{2}{\sum_i^n \rho_i l_i}}. \quad (30)$$

This expression is valid only for bypassed precipitates as it is independent of the applied stress. Indeed, all bypassed particles have the same strength and the dislocation must form a complete loop around the precipitate to break free. The average spacing is therefore simply the center-to-center distance between precipitates in the dislocation glide plane given by Eq. (30). However, in the case of shearable precipitates, this average spacing depends on the precipitate strength.

According to the Friedel statistics [42–44], the average spacing between shearable precipitates is given by Eq. (31):

$$\bar{L}_{sh} = \frac{1}{\sqrt{\rho_A \cos\left(\frac{\Phi_c}{2}\right)}}, \quad (31)$$

where  $\Phi_c$  is the strength of the precipitate expressed as its breaking angle, *i.e.* the critical angle to which a dislocation must bow out to unpin itself. Indeed, the precipitate is subject to the dislocation line tension,  $\Gamma$ , on both sides and its own resistance,  $F$ . The dislocation line forms an angle of  $\Phi_c$  around the precipitate at the unpinning moment. The equilibrium is such that Eq. (32) can be written:

$$F = 2\Gamma \cos\left(\frac{\Phi_c}{2}\right). \quad (32)$$

Combining Eqs. (26), (31) and (32) leads to the expression of the average spacing between precipitates for the case of shearable precipitates (Eq. (33)):

$$\bar{L}_{sh} = \sqrt{\frac{\sqrt{3}\Gamma}{F}} \bar{L}. \quad (33)$$

Finally, the set of equations presented so far leads to the expression of the contributions of shearable and bypassed precipitates to the yield stress of the material. By assuming a constant dislocation line tension  $\beta\mu b^2$ , Eqs. (34) and (35) can be obtained to evaluate the hardening coming from sheared and bypassed precipitates:

$$\sigma_{sh} = M\mu \left( k \frac{\sum_{i < i_c} \rho_i R_i}{\sum_{i < i_c} \rho_i} \right)^{3/2} \left( \frac{\sum_{i < i_c} \rho_i l_i}{2\sqrt{3}\beta b} \right)^{1/2}, \quad (34)$$

$$\sigma_{by} = \sqrt{2}M\beta\mu b \left( \sum_{i > i_c} \rho_i l_i \right)^{1/2}. \quad (35)$$

The parameters of the yield stress model are summarized in Table 6.

Table 6: Yield stress model parameters and the values used in this work.

Model parameter	Symbol	Value	Unit	Source
Burgers vector magnitude	$b$	$2.86 \times 10^{-10}$	m	[37]
Scale transition factor	$M$	2.24	-	[45]
Scaling factor	$\beta$	0.28	-	[6, 46, 47]
Intrinsic strength	$\sigma_0$	20	MPa	This work
Mg SSSC <sup>1</sup> scaling factor	$k_{Mg}$	342	MPa/at% <sup>2/3</sup>	[40]
Si SSSC <sup>1</sup> scaling factor	$k_{Si}$	137	MPa/at% <sup>2/3</sup>	[40]
Critical radius for shearing	$R_{crit}$	2.25	nm	This work

<sup>1</sup> solid solution strengthening contribution.

The yield stress model was calibrated against tensile test results using samples of the T7 heat treated A356+0.5wt.%Cu alloy aged at 200 °C during 0.1, 1, 10 and 100 h (same conditions as for the precipitation study). The tests were performed on a MTS servo-hydraulic tensile test machine. The samples and the grips used to secure them to both ends of the machine were designed specifically for these tests. The test sequence was displacement-controlled at a rate of 0.06 mm s<sup>-1</sup>. A reduced section diameter of 6 mm was chosen to eliminate any potential scale effects and obtain representative data. Each test was repeated three times for statistical validity. Therefore, a total of 12 tests was carried out. The engineering stress-strain curves were corrected for machine and grips compliance. Figure 10a shows the comparison between the simulated evolution of yield stress and the experimental results. Note that the dotted lines represent, from left to right, the end of quenching (from around 500 °C to room temperature), the beginning of heating (from room temperature to 200 °C) and the beginning of the holding at aging temperature (200 °C).

The fit strategy focused on having the model adequately represent the conditions in which the dominant strengthening precipitates are  $\beta''$  (*cf.* Table 3). This corresponds to the first three data points for which the durations of aging at 200 °C were 0.1, 1 and 10 hours. Indeed, it was shown in the TEM study that the condition aged for 100 hours showed a predominance of the Q-phase hardening precipitates. The fitting parameter here is the critical radius for shearing  $R_{crit}$  which was set at 2.25 nm to give the best possible fit.

Figure 10a shows how, with the exception of the condition aged for 0.1 h, the model is in good agreement with the experimental values and the aging curve is adequately represented. The model predicts a significantly lower yield stress for the condition aged for 100 hours compared to the experiments. This is easily explained by the phase transformation occurring at long aging durations which switches the main hardening system

from  $\beta''$  to Q and it is well known that the coarsening of Q-based precipitate is substantially slower than  $\beta$  precipitate. The model does not contain any consideration of this phase transformation and the evolution of the yield stress at longer aging durations is strictly controlled by the coarsening process. Peak hardness is reached after 3 hours of aging at 200 °C with a value of yield stress of approximately 280 MPa. After the peak, the yield stress decreases to a value of  $\sim 150$  MPa after 100 hours of aging. The yield stress follows the precipitate hardening contribution as it is the dominant mechanism. This contribution sharply increases in two stages which are in phase with the nucleation peaks. The less significant solid solution strengthening contribution evolves in the opposite sense since solute atoms take part in forming the precipitates, albeit at a small effect.

Figure 10b shows a breakdown of the contribution of precipitates into its two components (shearable and bypassed). This breakdown helps further understanding the reason behind the inability of the model to fit the first experimental data point. Indeed, a sharp peak in the contribution of shearable precipitates is observed in the first moments of the aging process. It corresponds to a large number of small - and therefore shearable - precipitates formed during the short aging durations leading to an abrupt increase in yield stress. Such a result reveals that the model cannot give a reliable quantitative description of yield stress evolution for short aging times. It seems that other type of precipitates and/or other type of micromechanical model should give better quantitative description for such conditions.

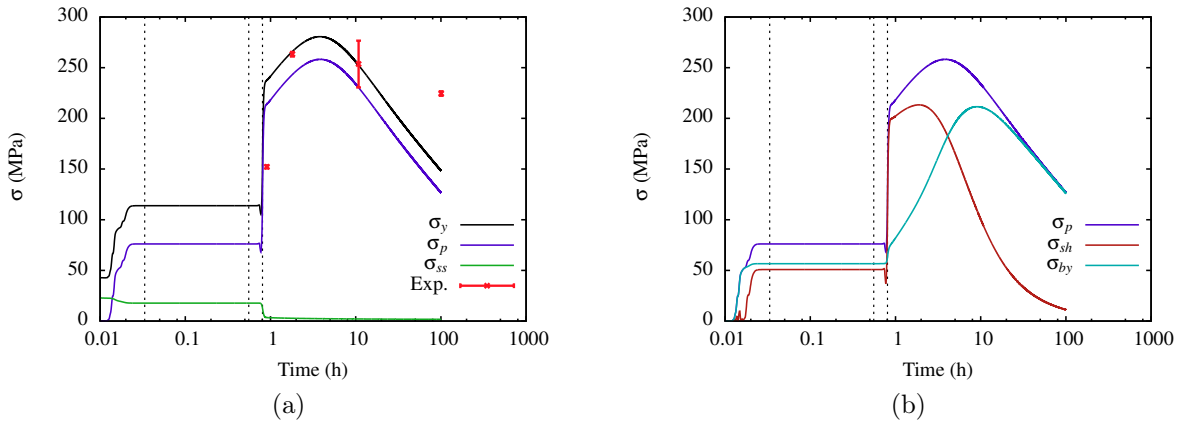


Figure 10: Fitting of the simulated yield stress ( $\sigma_y$ ) to experimental values (in red) using an  $R_{crit}=2.25$  nm: (a) breakdown of the evolution of each contribution and (b) breakdown of the contribution of precipitates into shearable and bypassed.

The goal of this computation chain, from precipitation to determination of the yield strength, is to eventually be coupled to the finite element method in order to perform calculations on cast aluminum parts. That will enable the study of the effect of heat treat parameters on, among other things, the gradient of yield strength and the prediction of residual stress.

## 6 Concluding remarks

This work was centered around modelling precipitation hardening in an A356+0.5wt.%Cu cast aluminum alloy for cylinder head applications. The main results can be summarized as follows:

- The use of TEM characterization shows that for short aging durations at 200 °C (up to 10 hours), the dominating hardening precipitates is  $\beta''$  rods, while for the long aging duration (up to 100 hours), the dominance shifts to the Q-phase system (Q', Q'' precipitates). The length and diameter of the  $\beta''$  rods were measured to produce size distributions.
- The precipitation model relies on classical nucleation/growth/coarsening equations. Indirect coupling to the Thermo-Calc software is used to input into the model essential thermodynamic variables such as the driving force for precipitation and the solubility product. The matrix/precipitate interfacial energy is treated as a fitting parameter. In this work two separate values are used: one for the nucleation equations and another for growth equations.
- Correction of the growth rate as well as curvature effect are implemented into the constitutive equations in order to take into account the elongated morphology of precipitates.
- The precipitation model is capable of reproducing the experimental size distributions with good accuracy.
- The yield stress is modelled as the Pythagorean sum of the contributions of intrinsic strength, solid solution strengthening and precipitation hardening. The major contribution being the one provided by precipitation hardening. The results of the yield stress model are also calibrated to experiments using the critical radius for shearing as a fitting parameter. With reasonable values of this parameter, a good agreement with the experiments was obtained.

An underestimation of yield stress was obtained for a long aging duration at 200 °C (100 hours). This is explained by the phase transformation observed during the microstructural analysis after long aging. Indeed, the transition to the Q-phase hardening system occurs and allows the alloy to maintain a higher level of yield stress for a significantly longer aging time.

Overall, this hybrid physics-based and phenomenological approach goes in the direction of the integrated computational materials engineering. A series of assumptions is made. They are accommodated by the use of fit parameters, the values of which could be detached from physical considerations. Finally, the physical underpinning of many aspects of this modelling effort offers a good scope of application, especially when compared to purely phenomenological approaches [2, 3, 48]. Indeed, thanks to this model, the effect of heat treatment parameters can be studied, the ability to handle non-isothermal states being at the core of the capabilities of this approach.

It is also possible to study, to a certain extent, the effect of changes in the chemical composition of the alloy. This is only limited by the necessity for the composition change to have no impact on the nature of the hardening precipitates.

This leads to the statement of the most important perspective of this work, which is the generalization to a multi-phase model. This should especially address the case where the precipitation of different phases is inter-dependent, such as for alloys of type A356+0.5wt.%Cu. The KWN approach is intrinsically capable of handling multiple distributions of precipitates, but the thermodynamic description of these phases and the transition from one to the other requires further work. More immediate perspectives

include the introduction of an evolution law for the aspect ratio, considered constant in this work, compatible with isothermal treatments.

From a more fundamental point of view, the experimental or computational determination of the matrix/precipitate interfacial energies would solve a major drawback of these approaches.

## Acknowledgements

Xiang Wang and Hatem Zurob are gratefully acknowledge for conducting TEM characterizations. Hervé Plancke is gratefully acknowledged for casting the tensile samples. Denis Massinon is gratefully acknowledged for providing technical support.

## Data availability

The raw/processed data required to reproduce these findings cannot be shared at this time due to legal or ethical reasons.

## References

- [1] Mustafa Kemal Kulekci. Magnesium and its alloys applications in automotive industry. *The International Journal of Advanced Manufacturing Technology*, 39(9-10):851–865, 2008.
- [2] Eric Nicouveau-Bourles. *Etude expérimentale et numérique du vieillissement d'un alliage d'aluminium. Application aux culasses automobiles*. PhD thesis, École Nationale Supérieure des Mines de Paris, 1999.
- [3] Bruno Barlas. *Etude du comportement et de l'endommagement en fatigue d'alliages d'aluminium de fonderie*. PhD thesis, École Nationale Supérieure des Mines de Paris, 2004.
- [4] John Allison, Dan Backman, and Leo Christodoulou. Integrated computational materials engineering: a new paradigm for the global materials profession. *Jom*, 58(11):25–27, 2006.
- [5] Rémi Martinez. *Modélisation multi-échelle des propriétés mécaniques d'un alliage d'aluminium de fonderie*. PhD thesis, Paris Est, 2012.
- [6] D. Bardel, M. Perez, D. Nelias, A. Deschamps, C.R. Hutchinson, D. Maisonnette, T. Chaise, Josselin Garnier, and F. Bourlier. Coupled precipitation and yield strength modelling for non-isothermal treatments of a 6061 aluminium alloy. *Acta Materialia*, 62:129–140, 2014.
- [7] Yue Li, Bjørn Holmedal, Hongxiang Li, Linzhong Zhuang, Jishan Zhang, and Qiang Du. Precipitation and strengthening modeling for disk-shaped particles in aluminum alloys: Size distribution considered. *Materialia*, 4:431–443, 2018.

- [8] Rui Chen, Qingyan Xu, Huiting Guo, Zhiyuan Xia, Qinfang Wu, and Baicheng Liu. Modeling the precipitation kinetics and tensile properties in Al-7Si-Mg cast aluminum alloys. *Materials Science and Engineering: A*, 685:403–416, 2017.
- [9] Shahrzad Esmaeili. *Precipitation hardening behaviour of AA6111*. PhD thesis, University of British Columbia, 2002.
- [10] V. Vaithyanathan, C. Wolverton, and L.Q. Chen. Multiscale modeling of  $\theta'$  precipitation in Al–Cu binary alloys. *Acta Materialia*, 52(10):2973–2987, 2004.
- [11] Zhiqiang Han, Guomin Han, Alan A. Luo, and Baicheng Liu. Large-scale three-dimensional phase-field simulation of multi-variant  $\beta$ -mg<sub>17</sub>al<sub>12</sub> in mg–al-based alloys. *Computational Materials Science*, 101:248–254, 2015.
- [12] S. Schmauder and P. Binkele. Atomistic computer simulation of the formation of Cu-precipitates in steels. *Computational Materials Science*, 24(1):42–53, 2002.
- [13] Atsuto Seko, Shigeto R. Nishitani, Isao Tanaka, Hirohiko Adachi, and Eiichi F. Fujita. First-principles calculation on free energy of precipitate nucleation. *Calphad*, 28(2):173–176, 2004.
- [14] R. Martinez, D. Larouche, G. Cailletaud, I. Guillot, and D. Massinon. Simulation of the concomitant process of nucleation-growth-coarsening of Al<sub>2</sub>Cu particles in a 319 foundry aluminum alloy. *Modelling and Simulation in Materials Science and Engineering*, 23(4), 2015.
- [15] Anass Assadiki, Vladimir A. Esin, Miguel Bruno, and Rémi Martinez. Stabilizing effect of alloying elements on metastable phases in cast aluminum alloys by CALPHAD calculations. *Computational Materials Science*, 145:1 – 7, 2018.
- [16] Thomas H. Ludwig, Paul L. Schaffer, and Lars Arnberg. Influence of vanadium on the microstructure of A356 foundry alloy. *Light Metals*, 2013.
- [17] George W. Smith. Precipitation kinetics in an air-cooled aluminum alloy: a comparison of scanning and isothermal calorimetry measurement methods. *Thermochimica acta*, 313(1):27–36, 1998.
- [18] Delavand Ovono-Ovono. *Recyclabilité des alliages d'aluminium de fonderie: Influence des éléments résiduels sur la microstructure et le comportement mécanique*. PhD thesis, Université Technologique de Compiègne, 2004.
- [19] Yan Zheng, Wenlong Xiao, Sujing Ge, Weitao Zhao, Shuji Hanada, and Chaoli Ma. Effects of Cu content and Cu/Mg ratio on the microstructure and mechanical properties of Al–Si–Cu–Mg alloys. *Journal of Alloys and Compounds*, 649:291–296, 2015.
- [20] Andrew Bobel, Kyoungdoc Kim, Christopher Wolverton, Mike Walker, and Gregory B. Olson. Equilibrium composition variation of Q-phase precipitates in aluminum alloys. *Acta Materialia*, 138:150 – 160, 2017.

- [21] Kyoungdoc Kim, Andrew Bobel, Sung-Il Baik, Mike Walker, P.W. Voorhees, and G.B. Olson. Enhanced Coarsening Resistance of Q-phase in Aluminum alloys by the addition of Slow Diffusing Solutes. *Materials Science and Engineering: A*, 735:318 – 323, 2018.
- [22] Xiang Wang, Shahrzad Esmaeili, and David J. Lloyd. The sequence of precipitation in the Al-Mg-Si-Cu alloy AA6111. *Metallurgical and materials transactions A*, 37(9):2691–2699, 2006.
- [23] D.J. Chakrabarti, Yingguo Peng, David E. Laughlin, et al. Precipitation in Al-Mg-Si alloys with Cu additions and the role of the Q' and related phases. In *Materials Science Forum*, volume 396, pages 857–862. Transtec Publications; 1999, 2002.
- [24] Kenneth C. Russell. Nucleation in solids: the induction and steady state effects. *Advances in Colloid and Interface Science*, 13(3-4):205–318, 1980.
- [25] John Wyrill Christian. *The theory of transformations in metals and alloys. I. Equilibrium and general kinetic theory*. Pergamon, 1975.
- [26] Bjørn Holmedal, Elisa Osmundsen, and Qiang Du. Precipitation of non-spherical particles in aluminum alloys part I: generalization of the Kampmann–Wagner numerical model. *Metallurgical and Materials Transactions A*, 47(1):581–588, 2016.
- [27] O.R. Myhr, Ø Grong, and S.J. Andersen. Modelling of the age hardening behaviour of Al–Mg–Si alloys. *Acta Materialia*, 49(1):65–75, 2001.
- [28] O.R. Myhr, Ø Grong, H.G. Fjaer, and C.D. Marioara. Modelling of the microstructure and strength evolution in Al–Mg–Si alloys during multistage thermal processing. *Acta Materialia*, 52(17):4997–5008, 2004.
- [29] Myriam Nicolas and Alexis Deschamps. Characterisation and modelling of precipitate evolution in an Al–Zn–Mg alloy during non-isothermal heat treatments. *Acta Materialia*, 51(20):6077–6094, 2003.
- [30] Aude Simar, Yves Bréchet, B. De Meester, A. Denquin, and Thomas Pardoen. Sequential modeling of local precipitation, strength and strain hardening in friction stir welds of an aluminum alloy 6005A-T6. *Acta Materialia*, 55(18):6133–6143, 2007.
- [31] Michel Perez. Gibbs–Thomson effects in phase transformations. *Scripta materialia*, 52(8):709–712, 2005.
- [32] Qiang Du, Bjørn Holmedal, Jesper Friis, and Calin D Marioara. Precipitation of non-spherical particles in aluminum alloys part II: numerical simulation and experimental characterization during aging treatment of an Al-Mg-Si alloy. *Metallurgical and Materials Transactions A*, 47(1):589–599, 2016.
- [33] Q. Du, W.J. Poole, M.A. Wells, and N.C. Parson. Microstructure evolution during homogenization of Al–Mn–Fe–Si alloys: Modeling and experimental results. *Acta Materialia*, 61(13):4961–4973, 2013.
- [34] Qiang Du, Michel Perez, Warren J. Poole, and Mary Wells. Numerical integration of the Gibbs–Thomson equation for multicomponent systems. *Scripta Materialia*, 66(7):419–422, 2012.

- [35] Richard Wagner, Reinhard Kampmann, and Peter W Voorhees. Homogeneous second-phase precipitation. *Phase transformations in materials*, 5:309, 2001.
- [36] O.R. Myhr and Øystein Grong. Modelling of non-isothermal transformations in alloys containing a particle distribution. *Acta Materialia*, 48(7):1605–1615, 2000.
- [37] C. Ravi and C. Wolverton. First-principles study of crystal structure and stability of Al–Mg–Si–(Cu) precipitates. *Acta materialia*, 52(14):4213–4227, 2004.
- [38] Yong Du, Y.A Chang, Baiyun Huang, Weiping Gong, Zhanpeng Jin, Honghui Xu, Zhaohui Yuan, Yong Liu, Yuehui He, and F.-Y Xie. Diffusion coefficients of some solutes in fcc and liquid Al: critical evaluation and correlation. *Mater. Sci. Eng. A*, 363(1):140–151, 2003.
- [39] A. de Vaucorbeil, W.J. Poole, and C.W. Sinclair. The superposition of strengthening contributions in engineering alloys. *Mater. Sci. Eng. A*, 582:147–154, 2013.
- [40] G.P.M. Leyson, L.G. Hector Jr., and W.A. Curtin. Solute strengthening from first principles and application to aluminum alloys. *Acta Materialia*, 60(9):3873–3884, 2012.
- [41] A. Deschamps and Y. Bréchet. Influence of predeformation and ageing of an Al–Zn–Mg alloy - II. Modeling of precipitation kinetics and yield stress. *Acta Mater.*, 47:293, 1999.
- [42] J. Friedel. *Dislocations*. Addison-Wesley Publishing Company Inc., Reading, Massachusetts, USA, 1964.
- [43] R.L. Fleischer and W.R. Hibbard. The relation between the structure and mechanical properties of metals. *Her Majesty's Stationary Office, London*, 261, 1963.
- [44] A.J. Ardell. Precipitation hardening. *Metall. Trans.*, 16A:2131, 1985.
- [45] G. Sachs and J. Weerts. Tensile tests on gold-silver crystals. *Z. Physik*, 1930.
- [46] C. Gallais, A. Denquin, Y. Bréchet, and G. Lapasset. Precipitation microstructures in an AA6056 aluminium alloy after friction stir welding: Characterisation and modelling. *Materials Science and Engineering: A*, 496(1-2):77–89, 2008.
- [47] Aude Simar, Yves Bréchet, B. De Meester, Anne Denquin, Christophe Gallais, and Thomas Pardoën. Integrated modeling of friction stir welding of 6xxx series Al alloys: process, microstructure and properties. *Progress in Materials Science*, 57(1):95–183, 2012.
- [48] François-Xavier Hoche. *Vers une prise en compte du vieillissement thermique dans la filière de dimensionnement des structures pour la fatigue thermomécanique*. PhD thesis, Paris Sciences et Lettres, 2016.